Eur. Phys. J. A **16**, 159–169 (2003)
DOI 10.1140/epja/i2000-10158-9

THE EUROPEAN PHYSICAL JOURNAL A

Narrow $\alpha + {}^{28}$Si elastic-scattering states at high excitation in ^{32}S

K.-M. Källman[1,a], M. Brenner[1], V.Z. Goldberg[2], T. Lönnroth[1], P. Manngård[1,b], A.E. Pakhomov[2], and V.V. Pankratov[2]

[1] Department of Physics, Åbo Akademi, FIN-20500 Turku, Finland
[2] Russian Scientific Center "Kurchatov Institute", 123182 Moscow, Russia

Received: 26 June 2000 / Revised version: 13 June 2002 /
Published online: 4 February 2003 – © Società Italiana di Fisica / Springer-Verlag 2003
Communicated by D. Guerreau

Abstract. The excitation function and angular distributions of elastic α-particle scattering on ^{28}Si have been measured in the laboratory energy range 6–28 MeV using a backscattering technique on a thick target, yielding a continuous energy distribution. More than 200 narrow states are observed, with widths in the range $\sim$ 30–100 keV at excitation energies $E^* = 13$–32 MeV. Angular distributions at backward angles were measured, and angular momentum values of more than 83 states have been deduced. The analysis gives spin-parities J^π, α-partial widths Γ_α and reduced widths of the narrow high-lying resonant states in ^{32}S. The experimentally observed states display both the negative- and the positive-parity rotational-like sequences with seemingly no parity splitting, a finding which is at variance with most potential-model predictions. The deduced effective moment of inertia indicates a more extended structure than the ground-state configuration. The observed strength of each ℓ-value is analyzed in terms of an underlying split doorway state of Lorentzian form, which yields an interpretation as fragmented rotational $\alpha + {}^{28}$Si states.

PACS. 21.10.Hw Spin, parity, and isobaric spin – 24.10.-i Nuclear-reaction models and methods – 24.30.-v Resonance reactions – 25.55.-e ^{3}H-, ^{3}He-, and ^{4}He-induced reactions

1 Introduction

There is an increasing interest in studying high-resolution elastic α-particle scattering in the mass range $A \sim 20$–40. The reason for this is the observation of narrow cluster structures, with $\Gamma_\alpha < 100$ keV, at excitation energies of tens of MeV [1], where potential scattering predicts structures with $\Gamma \sim 3-5$ MeV, but where the density of states is less than the density of compound-nucleus states.

In the $A \sim 20$–40 mass region α-particle elastic-scattering experiments range from a comprehensive study of ^{20}Ne states in [2], of excited states in ^{24,26}Mg [3,4], to narrow states observed in $\alpha + {}^{40}$Ca [5]. The α-particle scattering on ^{28}Si has been studied at lower energies and short energy intervals in [6–11] and at higher energies but with lower resolution in [12–14]. The α-particle transfer reaction (^{6}Li, dα) has been used for ^{28}Si, ^{32}S and ^{36}Ar in [15–17], and in several works on ^{40}Ca, see [18] and references therein.

As a result of all investigations prior to this work the excitation functions for elastic α-scattering by ^{28}Si, producing states in ^{32}S, in the present energy region have only been reported in fairly limited manner. In an early study at our laboratory, cf. [19], it was shown that over a broad energy interval a large number of individual highly excited, but very narrow states (*i.e.* $\Gamma \sim 30$–80 keV), with unambiguous angular momenta could be identified, provided a high-resolution technique could be used. However, this implied sampling the excitation function in narrow energy steps, which is very time consuming. A method to cover the excitation function over a large energy interval, but maintaining the good resolution, was developed [20]. This method was also used in a work on the low-energy scattering, *i.e.* a few MeV above the Coulomb barrier of $\alpha + {}^{28}$Si [9], and it is discussed extensively in [21].

The present work reports on a high-resolution study of elastic α-particle scattering on ^{28}Si. Parts of our data have been presented previously, cf. [9,16,22–25]. In this work we show that a rather simple method, instead of the full R-matrix approach, can be efficiently used to gain first insight in the resonance structure. Section 2 will describe the experiments performed, and features of the data reduction, and in the last section we discuss the present results.

[a] e-mail: kkallman@abo.fi
[b] *Present address*: Swedish Polytechnic, FIN-65200 Vasa, Finland.

2 Experimental procedure and results

2.1 Energy spectra and excitation function

The elastic-scattering excitation functions and angular distributions were measured at the Åbo Akademi Accelerator Laboratory using the K-20 isochronous cyclotron in the particle energy range 12.0–19.6 MeV, at Uppsala University in the range of 6.5–12.8 MeV beam energy using beams from the Tandem van de Graaff accelerator at the Svedberg Laboratory, and at Oslo University in the α-particle energy range 19–30 MeV using the K-35 cyclotron. The beam energies were analyzed with a 105° analyzing magnet at Åbo Akademi, with a 90° magnet in Uppsala, and with a 50° analyzing magnet at Oslo University. The experimentally deduced beam energy widths were about 20, 10 and 50 keV, respectively. Consequently the set-ups allow studies of energetically narrow structures. The target was a 10 μm thick plate of natural silicon. The isotope abundances are ^{28}Si 92.2, ^{29}Si 4.7 and ^{30}Si 3.1%, respectively. Since in addition to the low abundances the (α, α_0) cross-sections on ^{29,30}Si are smaller by factors of 5 and 3, respectively [24,26,27], their contributions are negligible (down to about 1%). Further, the (α, p) cross-sections are small [22,28] and the detectors were biased to be almost transparent to protons.

The experiments were performed using our novel thick-target method, see [20], to measure excitation functions and angular distributions in α-particle scattering. It allows measuring the elastic-scattering excitation function in fairly large energy steps, and continuously in energy. The absolute restriction in beam energy step length is the location of the first-excited state, in the case of ^{28}Si the 2^+ state at 1.78 MeV. However, for total α-particle path lengths (path in and path out) in the target material of several hundreds of keV, and this also depends on beam energy, straggling becomes important, and will smear the structures under study. The path length out is, in addition, depending on the scattering angle. This effect therefore prohibits beam energy steps larger than $\sim$ 400 keV. With the target at 45° with respect to the beam direction, the broadening is about 2 keV per degree opening angle in the backward direction, whereas it is 30 keV per degree at 90°.

The partial spectra were corrected for energy loss in the target and matched by normalizing the intensity, see [20]. The excitation function of $\alpha + {}^{28}$Si so obtained is shown in fig. 1, as recorded by the detector at 173°. The low-energy part reported in [9], and a high-energy excitation function from [29] are included for completeness. The intrinsic detector resolution was about 20 keV, which means that observed experimental widths of about 40 keV may indeed be narrower (even less than 30 keV).

The excitation functions were measured with a set of seven detectors in three settings, giving 21 angular-distribution points in the angle range 107°–173°. The individual spectra were recorded at 3° angle intervals, and the collimators used correspond to an angle width of $\Delta\theta \sim 2°$. In fig. 2 we show the backward-angle spectrum in comparison with the summed excitation function from an angu-

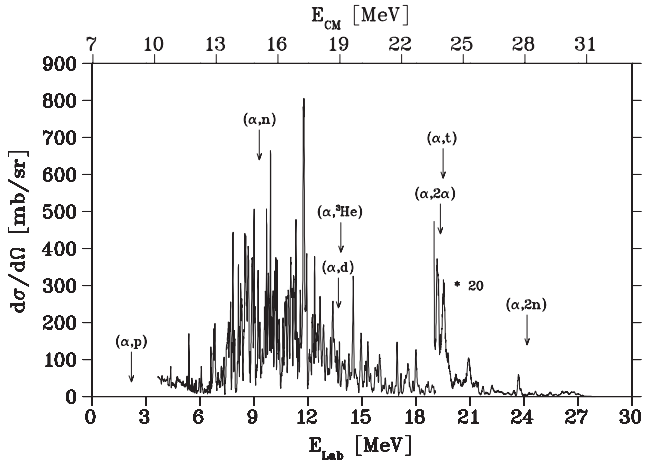

Fig. 1. Excitation function of the reaction $\alpha + {}^{28}$Si, in the energy range $E_\alpha \sim$ 3.6–30.0 MeV, corresponding to an excitation energy in the intermediate system ^{32}S of $E_{\rm exc}$ = 9.6–33.2 MeV. The excitation function is recorded at a laboratory angle of 173° with respect to the beam direction. The energy range $E_\alpha \sim$ 6.5–19.6 MeV is measured at the Tandem van de Graaff accelerator of the The Svedberg Laboratory in Uppsala and at the Turku cyclotron. Included are also the low-energy part, E_α = 3.6–5.8 MeV (*i.e.* $E_{\rm exc}$ = 9.6–12.2 MeV) from [9], and the high-energy part E_α = 19–30 MeV ($E_{\rm exc}$ = 23.6–33.2 MeV), recorded at the Oslo cyclotron [29]. Some particular reaction thresholds are indicated by arrows. It is interesting to notice that no appreciable changes in the elastic cross-section occur at or above these energy values.

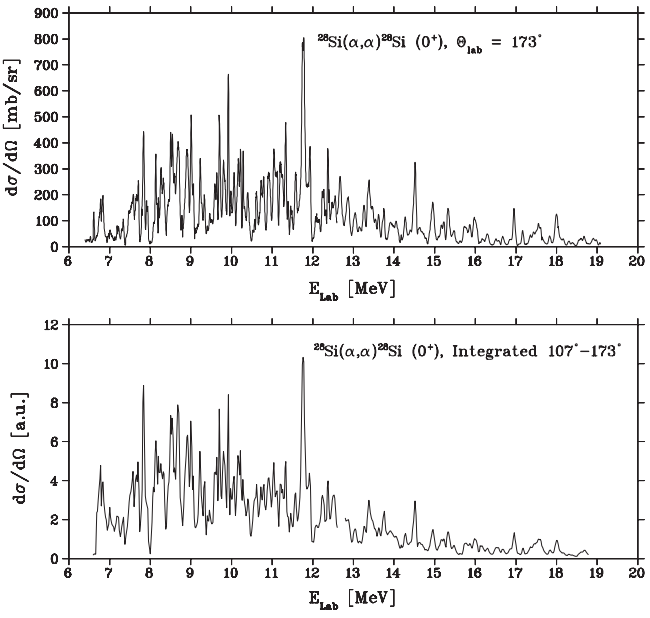

Fig. 2. Upper panel: backward-angle ($\theta_{\rm lab}$ = 173°) excitation function, cross-section in mb/sr. Lower panel: angle-summed ($\theta_{\rm lab}$ = 107°–173°) excitation function, in arbitrary units. The comparison illustrates that the observed structures are due to resonances, not fluctuations. A maintained excitation structure in the "integrated" spectrum indicates that the structure persists in the forward-angle interval and is not related with a fluctuating overlap of compound statistical resonances.

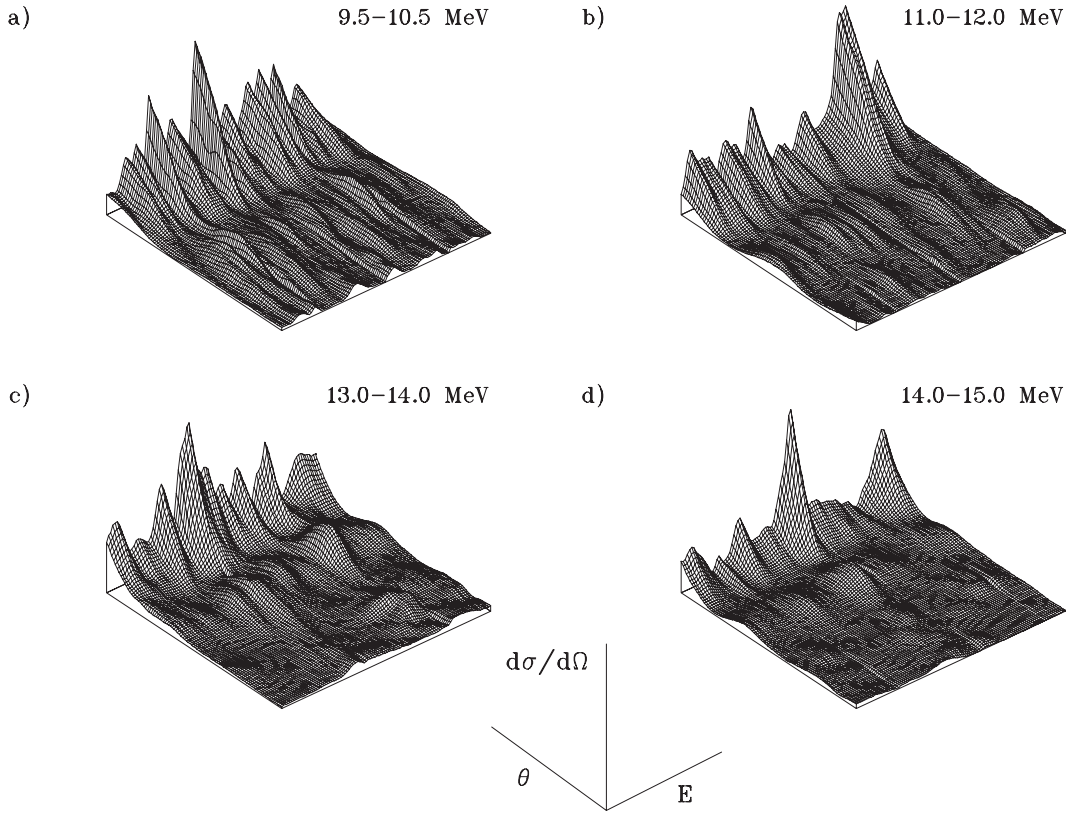

Fig. 3. Energy-angle matrices $E_{\rm CM} \times \theta_{\rm CM}$ extracted for four energy regions. It should be noted that the smooth energy and angle behaviors are not due to a model plot but the continuous energy is due to the experimental method, and only a splining of the $\Delta\theta \sim 3^\circ$ *angular* data has been done.

lar interval of 107°–173°. It should be noted how similar these two spectra are. The fact that there is some filling-in is mainly due to kinematic broadening at increasing angle off the beam direction. This feature is a signature that the observed states are not fluctuations but real resonances. This division in "backward intensity" and "integrated intensity" (which is, in fact, a sum of the in-plane intensity, see below for a discussion of the properties of the energy-angle $E_{\rm CM} \times \theta_{\rm CM}$ matrices) is of vital importance for the discussion of interference of partial waves.

2.2 Energy-angle matrices

The individual measured energy spectra for different angles were energy shifted and merged into two-dimensional $E_{\rm CM} \times \theta_{\rm CM}$ matrices. Examples of such energy-angle matrices are shown in fig. 3. (It should be noted, that projecting one such matrix on its energy axis yields a spectrum like that of the lower panel of fig. 2.) The four panels show parts of the total matrix with increasing energy. If there is low intensity observed in backward angles this may be due to the absence of scattering strength, *or* due to destructive interference of two (or more) partial waves. If however, there is in addition only a low in-plane intensity, *i.e.* low intensity in all angles, this is a sign that at this specific energy there is no resonance strength, only a low "background". This is illustrated in fig. 2, where it is easily recognized that, *e.g.*, at energies about 8.0, 8.4, 8.8, 9.1, 10.5, 12.0, etc. there is only "low-background" scattering, whereas in between there is a clear grouping of narrow resonances. The way we are going to use this procedure below presumes that the peaks are stronger than the potential-scattering background, so that the angular distribution is dominated by the ℓ-value of the resonant state. It seems plausible that this requirement is fulfilled. The partial fill-in in the angle-integrated spectrum is mostly due to kinematic broadening in smaller angles [20,21], otherwise the dips should be even lower. This effect is explained in detail in [20].

Since the resonances are reasonably well separated and appear as peaks above a background, cf. figs. 1 and 2 (upper panel), the excitation function was analyzed by fitting individual peaks with individual widths together with a background in the 173° spectrum. In this manner resonance energies and widths were extracted. Such a procedure should be well substantiated for separating out peaks which are fairly much higher than the background, and thus not suffering from interference in the backward angles, as seems to be the fact at energies larger than about 6 MeV. For lower energies, and down to the Coulomb barrier where Rutherford scattering dominates, the background interference is relatively stronger and here the data must be fitted including the background interference [9].

The total number of peaks analyzed is this way is almost 200 for the energy interval in consideration. Those with uniquely determined spin values (see below) are listed in table 1, with their positions and widths. The evolution of the experimental widths with increasing energy is such that there is a smooth increase in the mean widths from about 30 keV at 6 MeV, to some 70 keV at 20 MeV. This increase must be assigned to the resonant structures themselves, since the energy straggling in the target decreases with increasing beam energy and the relative beam energy width should stay constant [20].

2.3 Angular distributions

In the experimental two-dimensional data sets, illustrated in fig. 3, one can perform an angular-distribution analysis which is not restricted to preselected beam energy values of energy, rather, it allows slicing in energy at any interval. The slices were kept very narrow, typically 5–10 keV, in order to minimize the overlap with the wings of adjacent resonances.

The extraction of ℓ-values is done through slicing the matrix at certain energies, on the resonances determined from fits at backward angles, and projecting these angular distributions which are then compared to squared Legendre polynomials. If there is good agreement, the ℓ-value can be determined unambiguously. This is, in fact, the one-level approximation of the R-matrix theory. The present procedure is substantiated for reasonably well-separated and/or narrow resonances, which is often the case (see table 1), or for narrow slices projected at the resonance maximum, which minimizes the influence of wings from adjacent states.

This way of slicing was done for all peaks found in the analysis of the 173° spectrum, and for each case the width of the energy bin was chosen so as to avoid overlapping of adjacent resonances. For each energy, using the cross-section and the angular momentum of the resonance, one can get the characteristics, $\Gamma_\alpha/\Gamma_{\rm tot}$, of the corresponding state by use of the Breit-Wigner formula

$$\frac{{\rm d}\sigma}{{\rm d}\Omega} = \frac{1}{k^2}(2\ell+1)^2\frac{\Gamma_\alpha}{\Gamma_{\rm tot}}\cdot P_\ell^2(\cos\theta), \qquad (1)$$

where the angular dependence, given by the squared Legendre polynomial, determines the ℓ-value. Some examples of angular distributions so obtained are given in fig. 4. This comparison gives the dominating ℓ-values for each resonance, and are the ones listed in table 1.

Some uncertainties are present when using a single squared Legendre polynomial $P_\ell^2(\cos\theta)$ for deducing the ℓ-value. First, there may be two overlapping resonances, however, the expression is relatively insensitive to small admixtures. Second, the wings of adjacent resonances contribute, but at a distance of $\sim 3\Gamma$ the distortion is only marginal. For a resonance width of $\Gamma \sim 30$ keV, at a distance of 80 keV, the influence is small. Third, the small isotope admixture could distort the properties of weaker resonances. Fourth, one should include the Coulomb amplitude. However, it is very small for our energies, ~ 5 mb/sr or less and is neglected, especially since resonances with clear ℓ-values are fairly strong, some 50–500 mb/sr. Further, with increasing angle there is an increasing fill-in effect at minima (and lowering of peak values). This is an effect of kinematic broadening, compare to, *e.g.*, panels c) and d) of fig. 3. But as is seen, at angles close to 180° the agreement is good. Finally, admixtures of three different ℓ-values in one resonance may safely be excluded. They must be very occasional, and the trend, see fig. 5, clearly indicates successive ℓ-values with increasing energies, and not randomly appearing ones.

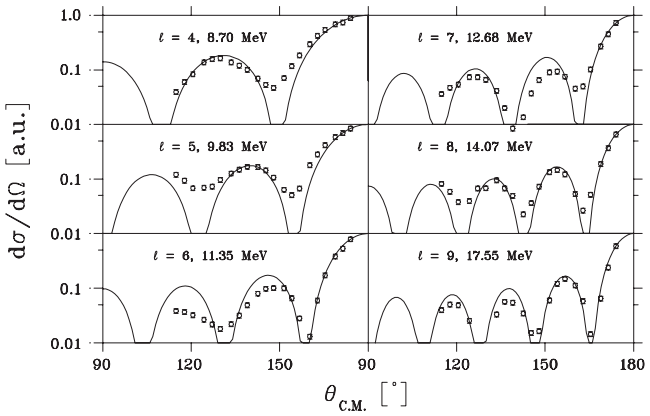

Fig. 4. Examples of experimental elastic α-particle angular distributions on ^{28}Si from the thick-target runs at various $E_{\rm CM}$ energies as shown in each plot. The spectra are obtained by slicing/gating in the $E_{\rm CM} \times \theta_{\rm CM}$ matrices shown in fig. 3. The theoretical curves represent $|P_\ell(\cos\theta)|^2$ Legendre polynomials.

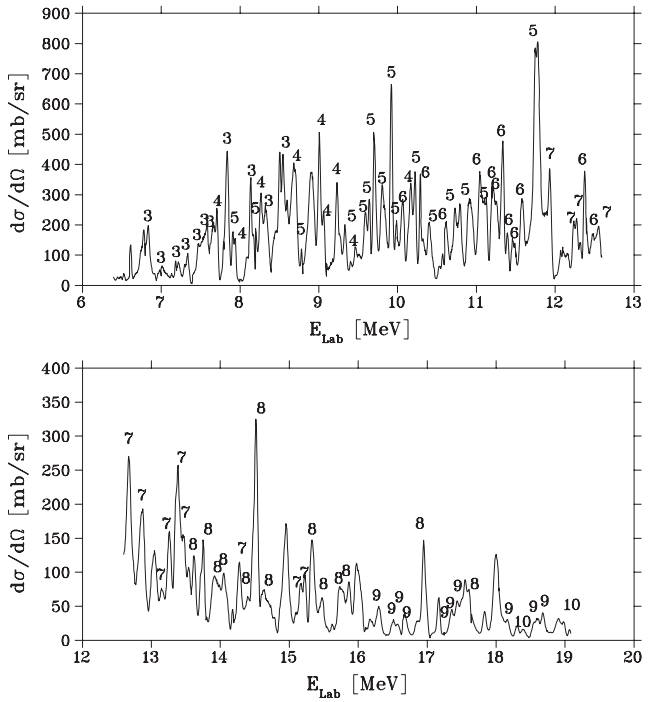

Fig. 5. Excitation function of the reaction $\alpha + {}^{28}$Si for the energy range $E_\alpha = 6.5$–19.6 MeV. The indicated numbers are the resonance ℓ-values extracted as discussed in the text.

Table 1. Properties of resonances observed in $\alpha + {}^{28}$Si elastic scattering at $\theta_{\rm lab} = 173°$. The columns represent the resonance energy $E_{\rm exc}$, laboratory energy $E_{\rm lab}$, ℓ-value, total width Γ, α-width Γ_α, relative width Γ_α/Γ, reduced width γ_α^2 and the percentage of the Wigner limit, $\gamma_\alpha^2/\gamma_{\rm W}^2$.

$E_{\rm exc}$	$E_{\rm lab}$	ℓ	Γ	Γ_α	Γ_α/Γ	γ_α^2	$\gamma_\alpha^2/\gamma_{\rm W}^2$
MeV	MeV		keV	keV			%
12.930	6.834	3	29 ± 5	16 ± 10	0.54	16 ± 10	2.7
13.086	7.012	3	26 ± 7	6 ± 4	0.24	5 ± 3	0.9
13.268	7.220	3	49 ± 3	17.9 ± 1.2	0.37	12.7 ± 0.8	2.1
13.370	7.337	3	28.8 ± 1.3	12.8 ± 0.8	0.44	8.6 ± 0.5	1.3
13.490	7.474	3	54 ± 5	28 ± 3	0.52	16.1 ± 1.7	2.6
13.588	7.586	3	18 ± 4	8 ± 2	0.42	4.0 ± 1.2	0.7
13.655	7.663	3	74 ± 2	50 ± 2	0.67	24.5 ± 0.9	4.0
13.696	7.710	4	23.6 ± 0.9	12.3 ± 0.6	0.52	14.1 ± 0.7	2.3
13.807	7.836	3	47.4 ± 0.8	27.9 ± 1.0	1.01	20.6 ± 0.4	3.4
13.870	7.908	5	22.0 ± 1.1	11.0 ± 0.6	0.50	10.5 ± 0.6	1.7
13.896	7.938	4	22.4 ± 1.0	8.8 ± 0.5	0.39	26.2 ± 1.4	4.3
14.070	8.137	3	29.6 ± 0.7	27.3 ± 0.8	0.92	9.6 ± 0.3	1.6
14.131	8.207	5	15.2 ± 0.6	6.6 ± 0.3	0.44	15.0 ± 0.7	2.4
14.177	8.259	4	42.0 ± 1.1	25.4 ± 1.1	0.61	18.1 ± 0.8	2.9
14.234	8.324	3	89 ± 2	69 ± 2	0.77	21.5 ± 0.5	3.5
14.429	8.547	3	40 ± 2	41 ± 2	1.02	11.8 ± 0.6	1.8
14.542	8.676	4	84.5 ± 1.1	66 ± 2	0.78	34.4 ± 0.8	5.6
14.633	8.780	5	7.0 ± 0.9	2.0 ± 0.3	0.28	2.6 ± 0.4	0.4
14.832	9.008	4	37.5 ± 0.5	33.2 ± 0.6	0.89	13.9 ± 0.3	2.3
14.878	9.060	4	25.5 ± 0.7	14.8 ± 0.5	0.58	6.0 ± 0.2	1.0
15.025	9.229	4	30.5 ± 1.1	21 ± 2	0.68	7.6 ± 0.6	1.2
15.116	9.332	5	36 ± 2	15.8 ± 1.4	0.44	13.6 ± 1.2	2.2
15.230	9.463	4	18 ± 2	5.1 ± 0.7	0.27	1.6 ± 0.2	0.3
15.344	9.593	5	45.9 ± 1.0	23.0 ± 0.7	0.50	16.5 ± 0.5	2.7
15.385	9.640	5	24.5 ± 0.6	13.6 ± 0.4	0.55	9.4 ± 0.3	1.5
15.441	9.704	5	34.3 ± 0.3	24.7 ± 0.5	0.72	16.4 ± 0.4	2.7
15.527	9.802	5	46.8 ± 1.3	24.8 ± 0.9	0.53	15.4 ± 0.6	2.5
15.631	9.921	5	29.9 ± 0.3	27.9 ± 0.4	0.93	16.0 ± 0.2	2.6
15.686	9.984	5	35.9 ± 1.0	16.7 ± 0.7	0.47	9.3 ± 0.4	1.5
15.758	10.066	6	41.0 ± 0.9	20.0 ± 0.6	0.49	32.2 ± 1.0	5.2
15.847	10.168	4	47 ± 2	33 ± 2	0.71	7.6 ± 0.6	1.2
15.894	10.222	5	28.0 ± 0.8	18.5 ± 0.7	0.66	8.8 ± 0.3	1.4
15.955	10.291	6	21.6 ± 0.5	14.4 ± 0.4	0.67	19.5 ± 0.6	3.2
16.052	10.402	5	54 ± 2	28 ± 2	0.52	12.0 ± 0.7	2.0
16.243	10.620	6	41.3 ± 0.8	18.8 ± 0.5	0.45	20.1 ± 0.5	3.3
16.341	10.732	5	86 ± 2	47.1 ± 1.4	0.55	17.1 ± 0.5	2.8
16.495	10.908	5	64 ± 3	39 ± 3	0.61	12.7 ± 1.0	2.1
16.615	11.046	6	60 ± 2	38 ± 2	0.63	30.3 ± 1.2	4.9
16.691	11.132	5	23 ± 2	12 ± 3	0.54	3.7 ± 0.8	0.6
16.747	11.197	6	45 ± 2	23 ± 3	0.52	17 ± 2	2.8
16.795	11.251	6	76 ± 6	41 ± 3	0.54	29 ± 2	4.8
16.866	11.333	6	38.1 ± 0.6	27.8 ± 0.6	0.73	18.8 ± 0.4	3.1
16.920	11.394	6	35.0 ± 0.8	14.4 ± 0.5	0.41	9.4 ± 0.3	1.5
16.978	11.461	6	47 ± 3	18 ± 2	0.38	11.0 ± 1.0	1.8
17.080	11.577	6	58.0 ± 1.4	32.5 ± 1.3	0.56	19.1 ± 0.7	3.1
17.250	11.771	5	92 ± 14	96 ± 27	1.04	22 ± 6	3.6
17.393	11.935	7	35 ± 6	20 ± 17	0.57	31 ± 26	5.0
17.656	12.235	7	36 ± 2	16.4 ± 0.8	0.45	20.6 ± 1.0	3.3
17.688	12.272	7	26 ± 2	10.8 ± 1.0	0.42	13.2 ± 1.2	2.1
17.868	12.478	6	82 ± 7	35 ± 3	0.43	13.1 ± 1.1	2.1
17.934	12.553	7	48 ± 4	20 ± 2	0.41	20 ± 2	3.3
18.042	12.677	7	44 ± 2	26.4 ± 1.2	0.61	25.3 ± 1.2	4.1
18.213	12.872	7	76 ± 7	28 ± 7	0.37	24 ± 6	4.0
18.458	13.152	7	66 ± 5	15.2 ± 1.2	0.23	11.2 ± 0.9	1.8
18.554	13.262	7	73.6 ± 1.4	28.3 ± 0.7	0.38	19.7 ± 0.5	3.2

Table 1. (Continued.)

$E_{\rm exc}$ MeV	$E_{\rm lab}$ MeV	ℓ	$\Gamma_{\rm exp}$ keV	Γ_α keV	Γ_α/Γ	γ_α^2	$\gamma_\alpha^2/\gamma_{\rm W}^2$ %
18.660	13.383	7	74 ± 5	38 ± 3	0.52	25 ± 2	4.1
18.736	13.470	7	75 ± 6	29 ± 2	0.39	18 ± 2	2.9
18.803	13.546	8	46 ± 3	12.9 ± 1.0	0.28	27 ± 2	4.4
18.986	13.755	8	34 ± 2	11.9 ± 1.0	0.35	22 ± 2	3.6
19.119	13.907	8	84 ± 7	23 ± 4	0.27	38 ± 6	6.2
19.248	14.055	8	54 ± 10	15 ± 3	0.27	23 ± 5	3.7
19.442	14.276	7	72 ± 2	25.4 ± 0.7	0.36	10.9 ± 0.3	1.8
19.551	14.401	8	75 ± 18	18 ± 4	0.24	22 ± 6	3.7
19.653	14.518	8	54 ± 2	31.6 ± 1.1	0.58	37.4 ± 1.3	6.1
19.747	14.625	8	79 ± 9	20 ± 3	0.25	22 ± 3	3.7
20.275	15.228	7	44 ± 4	15.1 ± 1.0	0.34	4.5 ± 0.3	0.7
20.381	15.350	8	72 ± 17	24 ± 10	0.33	18 ± 8	3.0
20.485	15.468	8	84 ± 4	20.8 ± 1.1	0.25	15.2 ± 0.8	2.5
20.703	15.718	8	37 ± 4	6.7 ± 1.0	0.18	4.4 ± 0.7	0.7
20.835	15.869	8	59 ± 2	16.5 ± 0.8	0.29	10.1 ± 0.5	1.6
21.212	16.299	9	69 ± 3	15.0 ± 0.8	0.22	25.6 ± 1.3	4.2
21.395	16.509	9	70 ± 5	11.2 ± 0.8	0.16	17.3 ± 1.2	2.8
21.457	16.579	9	45 ± 4	6.2 ± 0.7	0.14	9.2 ± 1.0	1.5
21.532	16.665	9	39 ± 10	6 ± 2	0.16	9 ± 6	1.5
21.783	16.952	8	53 ± 2	22.4 ± 0.8	0.42	8.9 ± 0.3	1.4
22.135	17.354	9	74 ± 4	14.9 ± 1.1	0.20	15.3 ± 1.2	2.5
22.205	17.434	9	54 ± 9	12 ± 4	0.22	12 ± 4	1.9
22.308	17.552	9	47 ± 14	10 ± 7	0.21	9 ± 6	1.5
22.355	17.606	8	24 ± 5	4.6 ± 1.3	0.19	1.4 ± 0.4	0.2
22.846	18.167	9	51 ± 5	8.3 ± 1.1	0.16	5.9 ± 0.8	1.0
22.964	18.395	10	58 ± 3	8.1 ± 0.6	0.14	20.3 ± 1.4	3.3
23.226	18.601	9	74 ± 16	14 ± 3	0.19	8 ± 2	1.3
23.296	18.681	9	52 ± 7	10 ± 2	0.20	6.3 ± 1.3	1.0
23.493	18.906	10	93 ± 12	17 ± 2	0.18	31 ± 4	5.1

In table 1 we have thus evaluated values only for resonances which are dominated by one component. (No attempt to fit several overlapping resonances, by virtue of a large number of parameters, has been done in the present work). There are altogether 84 states with definite ℓ-values, out of a total of 183 identified resonances, and there are some 40 additional ones in the high-energy data [29]. Examples of experimental angular distributions are displayed in fig. 4, in which the corresponding squared Legendre polynomials are included.

It is readily seen that many resonances clearly are dominated by one single ℓ-value (which fact also substantiates the peak-fitting analysis described above), whereas some contain interfering ℓ-values. Since one state can have only one angular momentum, this implies that all those "single resonances" that show interference indeed must be made up from at least two individual, overlapping states. This, in fact, means that the number of states in the energy region of study is larger than the number of "identified" states, 183. The excitation function at backward angles (173°), and deduced ℓ-values, is shown in fig. 5 for the energy region $E_{\rm lab} = 6.8$–18.9 MeV. For each angular momentum there are some 10 states or more with indicated ℓ-value in table 1, the widths of which are between 20 and 80 keV, as deduced from fits in the spectra.

2.4 Width analysis of "doorway states"

The elastic-scattering amplitude, $f(\theta)$, for scattering of alpha-particles by ^{28}Si can the be written

$$f(\theta) = f_{\rm C}(\theta) + f_{\rm N}(\theta), \tag{2}$$

where $f_{\rm C}$ is the Coulomb amplitude, and $f_{\rm N}(\theta)$ is the nuclear scattering amplitude, given by

$$f_{\rm N}(\theta) = \frac{i}{2k} \sum_\ell (2\ell+1) e^{2i\alpha_\ell} (1 - S_\ell) P_\ell(\cos\theta). \tag{3}$$

In this expression α_ℓ is the relative Coulomb phase, S_ℓ the scattering matrix element and $P_\ell(\cos\theta)$ a Legendre polynomial of order ℓ. The differential cross-section is then $\mathrm{d}\sigma/\mathrm{d}\Omega = |f(\theta)|^2$, and includes the interference of the nuclear and the Coulomb scattering amplitudes. The scattering matrix element S_ℓ can be written $S_\ell = \eta_\ell e^{2i\delta_\ell}$, where η_ℓ is the reflection coefficient, and δ_ℓ the nuclear phase shift.

For a resonance at $E = E_{\rm R}$ we have $\delta_\ell = \pi/2$, and $\cot\delta_\ell$ can be expanded in a Taylor series, and close to resonance we have [30]

$$\frac{i}{2}(1 - S_\ell) \sim \frac{\Gamma/2}{(E - E_{\rm R}) - i\Gamma/2}, \tag{4}$$

Table 2. Doorway states with spins J^π. The columns give the summed alpha widths Γ_α and reduced widths γ_α^2, the relative widths *vs.* the Wigner limit Γ_W, $\Sigma\gamma_\alpha^2/\Gamma_\mathrm{W}^2$, the centroid ϵ_0 (from a fit using expression (6)), the escape width $\Gamma^\uparrow$ and the spreading width $\Gamma^\downarrow$.

J^π	$\Sigma\Gamma_\alpha$ (keV)	$\Sigma\gamma_\alpha^2$ (keV)	$\Sigma\gamma^2/\Gamma_\mathrm{W}^2$	ϵ_0 (MeV)	$\Gamma^\uparrow$ (MeV)	$\Gamma^\downarrow$ (MeV)
3^-	322	150	0.24	7.75 ± 0.01	0.32 ± 0.01	0.88 ± 0.02
4^+	222	114	0.18	8.66 ± 0.01	0.34 ± 0.01	0.65 ± 0.01
5^-	404	217	0.35	10.20 ± 0.02	0.39 ± 0.03	1.63 ± 0.08
6^+	283	220	0.36	11.10 ± 0.01	0.29 ± 0.03	1.06 ± 0.05
7^-	273	224	0.36	13.20 ± 0.05	0.45 ± 0.04	1.84 ± 0.08
8^+	227	250	0.41	15.00 ± 0.02	0.41 ± 0.03	2.07 ± 0.09
9^-	108	118	0.19			
10^+	25	51	0.08			

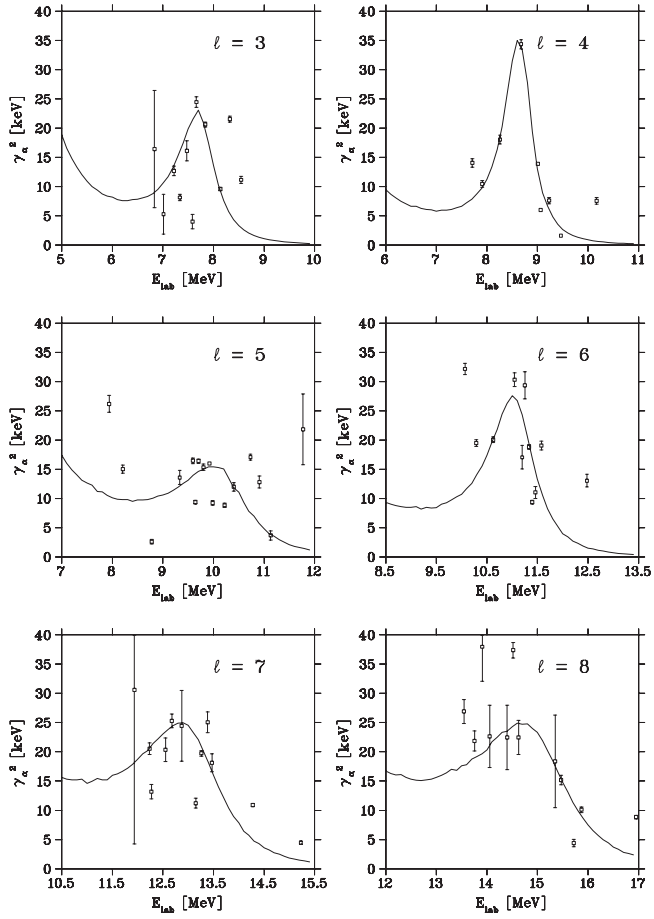

Fig. 6. Reduced widths γ_α^2 for fragments with the same spin, assuming an underlying doorway state, plotted as a function of energy. The solid lines in the graphs are fits to a Lorentzian shape, eq. (6). Note the non-linear behavior of the tails, which is due to the changing penetrability factor $P(a)$. See table 2 for numerical values.

where Γ is the width of the resonance. If other reaction channels than elastic scattering are open, Γ in the numerator is replaced with the alpha width Γ_α. When this expression is inserted in (3), the expression for $\mathrm{d}\sigma/\mathrm{d}\Omega = |f(\theta)^2|$ takes the form given in (1). The decay width Γ_α is related to the reduced width through $\Gamma_\alpha = 2P(a)\gamma_\alpha^2(a)$ [31], where $P(a)$ is the penetrability at channel radius a. The radius value $a = 5.4$ fm was used throughout. The reduced width γ_α^2 is often expressed as a dimensionless reduced width $\theta_\alpha^2(a)$ using the single-particle or Wigner limit $\gamma_\mathrm{W}^2 = \frac{3}{2}(\hbar^2/\mu a^2)$, that is

$$\theta_\alpha^2(a) = \frac{2\mu a^2}{3\hbar^2}\,\gamma_\alpha^2. \tag{5}$$

If the ratio θ_α^2 is close to unity, the state is interpreted as being an α-cluster state [32], *i.e.* a state containing most of the strength for that particular ℓ-value. The reduced widths γ_α^2 are plotted in fig. 6.

If the observed "fine structures", *i.e.* groups of narrow states with the same ℓ-values, are due to some kind of doorway state split into fragments, the individual alpha widths Γ_α should sum up to the escape width $\Gamma^\uparrow$ of this underlying doorway state [33], and the reduced widths should add up to the total width. The reduced widths as a function of energy should be given by a Lorentzian form,

$$\gamma_\alpha^2 = \frac{d}{4\pi\,P(a)}\,\frac{\Gamma^\uparrow\Gamma^\downarrow}{(E_\mathrm{lab}-\epsilon_0)^2 + \frac{1}{4}(\Gamma^\downarrow)^2}, \tag{6}$$

where d is the (mean) distance between the fragments, and ϵ_0 is the energy of the doorway state. The factor $\Gamma^\downarrow$ is called the spreading width, or decay width of the resonance, or doorway state. The distance d is assumed to be a constant for a given state, and $d = 200$ keV is used for the mean distance of analyzed states in table 1. The widths of the Lorentzian distributions of states with the same ℓ-value were fitted with the expression (6), and the fits are shown in fig. 6. From these calculations the values of the escape and spreading widths, $\Gamma^\uparrow$ and $\Gamma^\downarrow$, could be deduced. The numerical results of the width analyses are shown in table 2. It should be carefully remarked, however, that the values obtained only may be used as guide-line values. As pointed out earlier, half of the states do not have assigned ℓ-values, and additional (broad) states may still be missed, especially towards higher energy. The general expected trend of these states is described in figs. 22 and 23 of ref. [34]. The question about missing states and

their influence in conclusions will be re-addressed in subsect. 3.2 below.

In table 2 it should be especially noted that the sum of the reduced widths normalized to the Wigner limit, $\sum \gamma_\alpha^2/\gamma_{\rm W}^2$, reaches almost 50% in some cases. In view that we have not been able to determine the total strengths, that is, almost half of the resonances are without assigned ℓ-values, these values may well add up closely to 1. This is a clear indication that the states may be interpreted to be of α-cluster nature. One should carefully note, though, that the Wigner limit is fairly loosely defined. A change in the channel-radius value by some 20% changes the exhausting by almost 50%. However, the general picture is relatively clear.

3 Discussion

3.1 Potential analysis of the excitation function

The interaction between a particle and a nucleus is usually described by a local central complex optical potential. The real part is often parametrized with a Woods-Saxon form factor, or a W-S squared, for both real and imaginary parts. In the present work the potential is parametrized according the prescription of [35,36], who obtained a "universal potential" by fitting to data of $\alpha + {}^{16}$O and $\alpha + {}^{40}$Ca. This potential $U(r)$ has a squared Woods-Saxon shape

$$U(r) = -V\, f(r, R_V, a_V) - W\, f(r, R_W, a_W) \qquad (7)$$

where the form factors are given by $f(r, R_i, a_i) = 1/[1 + \exp(r - R_i/a_i)]^2$, where the indices are $i = V, W$ for the real and imaginary parts, respectively. The best parameter values for the present elastic $\alpha + {}^{28}$Si data, obtained from fits to angular distributions, were determined to be $V = 192.4(1 - 0.00173E_\alpha), W = -3.35(1 - 0.020E_\alpha), R_V = 1.45, R_W = 1.65, a_V = 1.2$ and $a_W = 1.0$, in units of MeV and fm. Note, thus, the energy dependences of the potential depths.

Figure 7 shows the excitation function calculated for the backward angle 173°, together with the measured data. As can be seen, there is generally good agreement for the overall behavior from about 6.5 to 19 MeV. However, as expected, the potential approach fails to reproduce the fine details. Included is also a curve obtained by smoothing the experimental data with a Gaussian of 400 keV width. Although the averaging is coarse from a statistical point of view there is still much structure in the smoothed curve, indeed, the structure disappears only for a smoothing of about 2 MeV. Thus the origin of the fine structures may be of non-statistical origin [27].

When the Woods-Saxon potential above is used to calculate the elastic-scattering cross-section *vs.* angle, one obtains a matrix like that shown in fig. 8. It is clearly seen that the structures are much broader in energy than those shown in fig. 3, which fact is reflected also the theoretical excitation function in fig. 7. The matrix is calculated

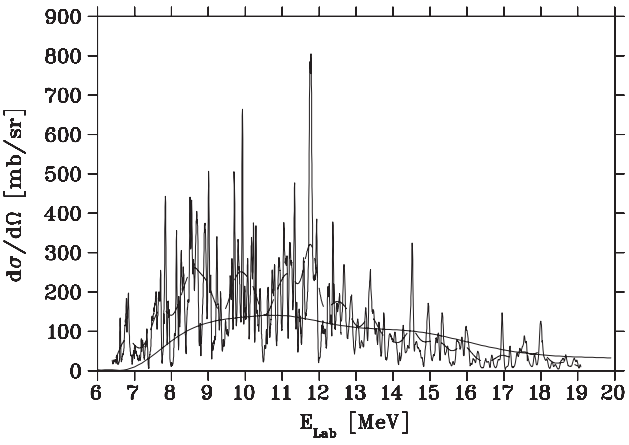

Fig. 7. Theoretical excitation function (full line) calculated with the potential form described in the text, superimposed on the experimental data to which the parameters were fitted. The smoothed experimental data (smoothing 400 keV) is also shown as the broken line.

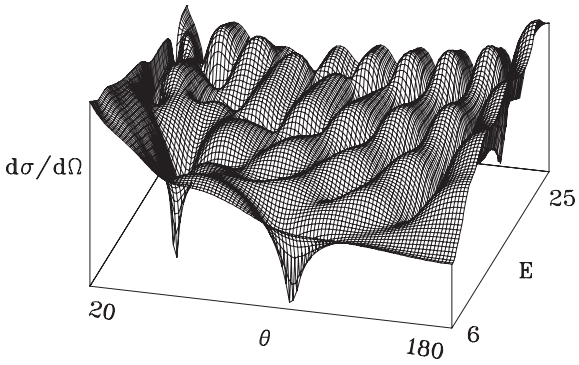

Fig. 8. Theoretical $E_{\rm CM} \times \theta_{\rm CM}$ matrix calculated with the same potential as used to produce fig. 7.

from 6 to 25 MeV, but only shows a few bulges, in contrast to the experimentally found about 180 narrow states. Also, even at 25 MeV the angular momentum is only $8\hbar$, whereas experimentally the values definitely seem higher, ~ 10–$12\hbar$. The potential thus only gives a fair description of the gross structure. In fact, the same kind of smooth-behavior presentation has been given for, *e.g.*, the $\alpha + {}^{40}$Ca case [37]. Novel aspects of the potential description have also been recently discussed in [38,39] for the $\alpha + {}^{28}$Si scattering.

3.2 Average dynamics

The states which have an unambiguously determined ℓ-value in table 1 (and fig. 5) are plotted in a phase-space diagram, that is an $E = \hbar^2/2\mathcal{J}\,[\ell(\ell+1)]$ graph in fig. 9. It is quite suggestive that the states with the same ℓ-values group according to increasing energies with a linear dependence on $\ell(\ell+1)$ and they are not, for one particular ℓ-value, spread over a large energy region. This fact is of importance since it is indicative of an average rotational behavior. The states of the figure consist of the

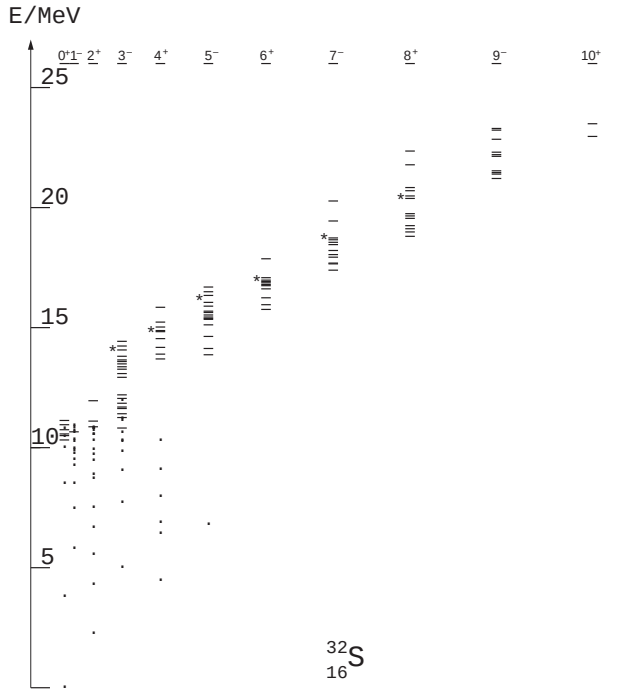

Fig. 9. Phase space diagram of observed states, that is, an $E = E[\ell(\ell+1)]$ graph, for those states that have determined ℓ- values in fig. 5. In addition the low-spin scattering states from [8], and "spectroscopic states" down left from [40] (marked with dots), are included for comparison. Due to accelerator calibration uncertainties some of the 0^+–3^- states of [9,40] may be the same. As is seen the moments of inertia for the two parities are almost the same, and there is no evidence for parity splitting. States marked "$\star$" are the centroids ϵ_0 reported in table 2.

low-lying (ground-band) states, and the 1^-–9^- and the 0^+–10^+ groups of the present analysis. The low-spin and low-energy levels are from [40].

The energy spectrum of a "molecular" rotational band of states with angular momenta ℓ is given by the well-known expression

$$E_{\rm rot} = E_0 + \frac{\hbar^2}{2\mathcal{J}}\,\ell(\ell+1), \tag{8}$$

with $E_0 = E_{\rm B} + E_{\rm C}$ being the "band head energy", where $E_{\rm B}$ is the binding energy of the α-particle in the target nucleus (the Q-value), and $E_{\rm C} = 1.21\,Z_1\,Z_2\,[r_0(A_1^{1/3} + A_2^{1/3}) + 0.5]^{-1}$ is the Coulomb energy. From fig. 9 the value $E_0 \sim 12.2$ MeV can be extracted. If the constituents α and ^{28}Si are considered to be extended (non–point-like) particles their combined moment of inertia $\mathcal{J}$ is calculated given by the expression replacing their masses by their mass numbers and their radii by the standard expression $R = r_0 \cdot A^{1/3}$. We arrive at the following expression for the moment of inertia of the combined $\alpha + {}^{28}$Si (that is, masses $A_1 + A_2$) system, in the limit of two osculating spheres [41]:

$$\mathcal{J}_{\rm mol} = 1.04 r_0^2 \left(\frac{2}{5}(A_1^{5/3} + A_2^{5/3}) + A_1 A_2 \frac{(A_1^{1/3} + A_2^{1/3})^2}{A_1 + A_2} \right) \tag{9}$$

in units of $\hbar^2$/MeV. For the present purpose we have used $r_0 = 1.3$ fm. The moment of inertia for the two constituents at touching distance is then $3.28 \cdot 10^{-42}$ MeVs^2 or $\mathcal{J}_{\rm mol} = 7.57\,\hbar^2$/MeV, whereas for a spherical mass with $A = 32$ it is $1.13 \cdot 10^{-42}$ MeVs^2, that is, $\mathcal{J}_{\rm spher} = 2.59\,\hbar^2$/MeV. Our experimental value, extracted from the $\ell(\ell+1)$ behavior of the weighted averages of the individual states with spin ℓ, is $\mathcal{J}_{\rm exp} \sim 4.5$–$5.0\,\hbar^2$/MeV. This effective moment of inertia corresponds to an object that is more elongated than the spherical one, but less than two osculating spheres, in accordance with the intuitive picture for the present process of an α-particle located at or in the nuclear surface.

The influence of missed states on the conclusions was mentioned in subsect. 2.4. For a particular ℓ-value the widths are cut at lower energies by the penetrability, see eq. (6), and for increasing energy the resonances become broader, and eventually constitute a smooth background, and in addition, at these energies members of the next ℓ-value begin to appear. These unobserved states should not change the general conclusions, but they would increase the number of states at higher energies for each ℓ-value in fig. 9.

Finally, we may turn to discuss the kR values of the observed states. The wave number is obtained from the mean energy within an ℓ-group, and the interaction radius is taken as the sum of the radii of the alpha-particle and the core nucleus, $R = (1.3A^{1/3} + 1.6)$ fm. It so turns out that the estimated grazing angular momenta $\ell_{\rm graz} = k \cdot R$ are in good accordance with the measured ones. This fact also suggests that the observed structures are due to a surface phenomenon. The argument then is also in accordance with the observation that with increasing energy the next ℓ-value appears.

3.3 Gamma-ray lifetimes

The experimental effective moment of inertia, $\mathcal{J}$, of a rotational band can be used to estimate (collective) γ-ray transition rates. In the liquid-drop framework [42] the moment of inertia and the quadrupole deformation parameter β_2 are related by the expression $\mathcal{J} = \beta_2^2 A^{7/3}/400$ MeV^{-1}. In the same way one can estimate the quadrupole transition rate $B(E2)$, given by $B(E2) = Q_0^2 \frac{15}{2\pi} F(I)$, where $Q_0 = \sqrt{\frac{16\pi}{5}} \frac{3}{4\pi} Z e R_0^2 \beta_2$ is the static quadrupole moment, and $F(I)$ is a spin factor. Substituting these expressions gives $B(E2) = \frac{675}{2\pi^2} Z^2 A^{-1} r_0^4 \cdot F(I) \cdot \mathcal{J}$ e^{2}fm^4. For the cluster band one then obtains the value $B(E2)_{\rm cluster} = 22.4$ e^{2}fm^4, for $I = 8$. This value can be compared to the single-particle value, or Weisskopf estimate, for $A = 32$, $B(E2)_{\rm s.p.} = 6.0$ e^{2}fm^4. The corresponding γ-ray transition rate is given by $T(E2) = 1.22 \cdot 10^9 E_\gamma^5 \cdot B(E2)$, and

the α-particle half-life can be estimated from the expression $\Gamma_\alpha \cdot \tau \sim \hbar$. Inserting numbers we obtain for the γ-ray and the α-cluster half-lives:

$$T_{1/2}^{\gamma,\mathrm{cluster}} \sim 2 \cdot 10^{-14}\mathrm{s}\,; \qquad T_{1/2}^{\alpha,\mathrm{cluster}} \sim 1 \cdot 10^{-18}\mathrm{s}\,. \quad (10)$$

That is, the probability for α-emission is more than 10^4 times greater than that for a γ-transition.

However, a γ-branch of about 10^{-4} or slightly less, should be observable with modern equipment, and in fact, two cases of γ-ray branching are known. A first report of this kind is given for a 10^+ state of ^{24}Mg populated in the reaction ^{12}C(^{12}C,α)^{20}Ne, at $E_{\mathrm{CM}} = 16.45$ MeV corresponding to $E_{\mathrm{exc}} = 30.38$ MeV [43]. Here the total γ-branch to a number of 8^+ states in the range $E_{\mathrm{CM}} =$ 8.85–12.98 MeV ($E_{\mathrm{exc}} = 22.78$–26.91 MeV), with $E_\gamma \simeq$ 6.9 MeV, is given as $(1.2 \pm 0.4) \cdot 10^{-5}$. This is indeed of the same order of magnitude as the crude liquid-drop estimate above.

Quite recently a second case is found, see [44]. The $\gamma - \alpha$ branching ratio of another 10^+ state in ^{24}Mg, at $E_{\mathrm{exc}} = 19.2$ MeV, is reported as $(7 \pm 3) \cdot 10^{-4}$. The $10^+ \to 8^+$ γ-ray energy is here 5.93 MeV. Although the two branching values agree with the rough liquid-drop estimate, the former has a much larger branching to α-emission, probably due to Q-value and barrier effects.

4 Summary and conclusions

It has been shown that excitation functions and angular distributions measured with the backscattering technique on a thick target give very interesting results. The extracted level properties, excitation energies, spins and parities, and widths in the resonance α-scattering seem to suggest an α-cluster or quasimolecular structure in $\alpha + {}^{28}$Si. When compared to similar findings in lighter nuclei, these results give support to the assumption that the formation of α-cluster quasimolecular structures is a general phenomenon in the interaction of alpha-particles with light nuclei.

We are indebted to Göran Possnert and the Tandem Accelerator Laboratory staff of Uppsala University for making the experiments there possible and for their help during the runs. We further acknowledge the grants from Jubileumsfonden 1968 at Åbo Akademi which enabled the travels to Uppsala. We are also indebted to the personnel of the Oslo Cyclotron Laboratory for the efficient help in the running. Finally, the financial support from the Academy of Finland (VZG, AEP and VVP) is gratefully acknowledged.

References

1. A.H. Wuosmaa, R.R. Betts, M. Freer, B.R. Fulton, Annu. Rev. Nucl. Part. Sci. **45**, 89 (1995).
2. J.H. Billen, Phys. Rev. C **20**, 1648 (1979).
3. R. Abegg, C.A. Davies, Phys. Rev. C **43**, 2523 (1991).
4. C.A. Davies, R. Abegg, Nucl. Phys. A **571**, 265 (1994).
5. D. Frekers, R. Santo, K. Langanke, Nucl. Phys. A **394**, 189 (1983).
6. W. Wühr, A. Hofmann, G. Philipp, Z. Phys. A **269**, 365 (1974).
7. J.J. Lawrie, A.A. Cowley, D.M. Whittal, S.J. Mills, W.R. MeMurray, Z. Phys. A **325**, 175 (1986).
8. H.B. Willard, J.K. Bair, Bull. Am. Phys. Soc. **7**, 73 (1962).
9. K.-M. Källman, Z. Phys. A **356**, 287 (1996).
10. H.-s. Chen, H. Shen, F. Yang, J.-y. Tang, Nucl. Instrum. Methods B **85**, 47 (1994).
11. H. Yonezawa, K. Shikano, T. Shigematsu, Nucl. Instrum. Methods B **88**, 207 (1994).
12. A. Bobrowska, A. Budzanowski, K. Grotowski, L. Jarczyk, B. Kamys, A. Kapucik, J. Ploskonka, A. Stralkowski, Z. Wrobel, L. Zastawniak, R. Zybert, Acta Phys. Pol. B **5**, 125 (1974).
13. A. Budzanowski, L. Jarczyk, B. Karnys, A. Kapucik, Nucl. Phys. A **265**, 462 (1976).
14. L. Jarczyk, B. Maciuk, M. Siemaszko, W. Zipper, Acta Phys. Pol. B **7**, 531 (1976).
15. K.P. Artemov, M.S. Golovkov, V.Z. Goldberg, V.I. Dukhanov, I.B. Mazurov, V.V. Pankratov, V.V. Paramonov, V.P. Rudakov, I.N. Serikov, V.A. Soloviev, V.A. Timofeev, Yad. Fiz. **51**, 1220 (1990) (English translation: Sov. J. Nucl. Phys. **51**, 7771 (1990)).
16. K.P. Artemov, M.S. Golovkov, V.Z. Goldberg, V.V. Pankratov, V.P. Rudakov, M. Brenner, P. Manngård, K.-M. Källman, T. Lönnroth, Yad. Fiz. **55**, 884 (1992) (English translation: Sov. J. Nucl. Phys. **55**, 4921 (1992)).
17. T. Yamaya, M. Saitoh, M. Fujiwara, T. Itahashi, K.Katori, T. Suehiro, S. Kato, S. Hatori, S. Ohkubo, Nucl. Phys. A **573**, 154 (1994).
18. T. Yamaya, K. Ishigaki, H. Ishiyama, T. Suehiro, S. Kato, M. Fujiwara, K. Katori, M.H. Tanaka, S. Kubono, V. Guimaraes, S. Ohkubo, Phys. Rev. C **53**, 131 (1996).
19. P. Manngård, M. Brenner, K.-M. Källman, T. Lönnroth, M. Nygård, V.Z. Goldberg, M.S. Golovkov, V.V. Pankratov, V.P. Rudakov, *Proceedings of the International Conference on Atomic and Nuclear Clusters, Åbo Akademi, Turku, June 3-7, 1991*, edited by M. Brenner, T. Lönnroth, F.B. Malik (Springer Verlag, Heidelberg, 1992) p. 377.
20. K.-M. Källman, V.Z. Goldberg, T. Lönnroth, P. Manngård, A.E. Pakhomov, V.V. Pankratov, Nucl. Instrum. Methods Phys. Res. A **338**, 413 (1994).
21. K.-M. Källman, Thesis (Department of Physics, Åbo Akademi, 1998, ISBN 952-12-0291-2).
22. M. Brenner, Z. Phys. A **349**, 233 (1994).
23. P. Manngård, Z. Phys. A **349**, 335 (1994).
24. P. Manngård, Thesis (Department of Physics, Åbo Akademi, 1996, ISBN 951-650-700-X).
25. A. Ludu, A. Sanduleseu, W. Greiner, K.-M. Källman, M. Brenner, T. Lönnroth, P. Manngård, J. Phys. G: Nucl. Part. Phys. **21**, L41 (1995).
26. A.E. Antropov, M. Brenner, V.Z. Goldberg, W. Greiner, K.-M. Källman, T. Lönnroth, A. Ludu, P. Manngård, A.E. Pakhomov, V.V. Pankratov, *Proceedings of the 7th International Conference on Nuclear Reaction Mechanisms, Varenna, 1994*, edited by E. Gadioli, Ricerca Scientifica ed Educazione Permanente, Supplemento **100**, 430 (1994).
27. M. Brenner, E. Indola, K.-M. Källman, T. Lönnroth, P. Manngård, M. Halldorsdottir, Th. Karlsson, Z. Máte, L. Zolnai, V.Z. Goldberg, G.V. Rogatchev, M.V. Rojkov, I.N. Serikov, W. Trzaska, R. Wolski, APH N.S., Heavy Ion Phys. **7**, 355 (1998).

28. K. Jankowski, A. Grzeszczuk, M. Siemaszko, A. Surowiec, W. Zipper, A. Budzanowski, E. Kozik, Nucl. Phys. A **426**, 1 (1984).
29. T. Lönnroth, K.-M. Källman, P. Manngård, unpublished.
30. D.F. Jackson, *Nuclear Reactions* (Chapman and Hall, London, 1970).
31. A.M. Lane, R.G. Thomas, Rev. Mod. Phys. **30**, 257 (1958).
32. K. Wildermuth, Y.C. Tang, *A Unifled Theory of the Nucleus* (Academic Press, New York, 1977).
33. C. Mahaux, H.A. Weidenmüller, *Shell-Model Approach to Nuclear Reactions* (North-Holland Publishing Company, 1969).
34. F. Michel, S. Ohkubo, G. Reidemeister, Prog. Theor. Phys., Suppl. **132**, 7 (1998).
35. F. Michel, J. Albinski, P. Belery, Th. Delbar, Gh. Gregoire, B. Tasiaux, G. Reidemeister, Phys. Rev. C **28**, 1904 (1983).
36. F. Michel, G. Reidemeister, S. Ohkubo, Phys. Rev. C **34**, 1248 (1986); **37**, 292 (1988).
37. F. Michel, G. Reidemeister, Phys. Rev. C **29**, 1928 (1984).
38. A.S.B. Tariq, A.F.M.M. Rahman, S.K. Das, A.S. Mondal, M.A. Uddin, A.K. Basak, H.M. Sen Gupta, F.B.Malik, Phys. Rev. C **59**, 2558 (1999).
39. S.K. Das, A.S.B. Tariq, A.F.M. Rahman, R.K. Roy, M.N. Huda, A.S. Mondal, A.K. Basak, H.M. Sen Gupta, F.B. Malik, Phys. Rev. C **60**, 044617 (1999).
40. P.M. Endt, Nucl. Phys. A **521**, 1 (1990).
41. U. Abbondanno, Phys. Rev. C **43**, 1484 (1991).
42. P. Ring, P. Schuck, *The Nuclear Many-Body Problem* (Springer Verlag, New York, 1980).
43. F. Haas, A. Elanique, R.M. Freeman, C. Beck, C. Nouicer, D.L. Watson, C. Jones, R. Cowin, P. Lee, Z. Basrak, Il Nuovo Cimento A **110**, 989 (1997).
44. I. Wiedenhöver, A.H. Wuosmaa, C.J. Lister, M.P. Carpenter, R.F.V. Janssens, H. Amro, J. Caggiano, A. Heinz, F.G. Kondev, T. Lauritsen, S. Siem, A. Sognoni, M. Devlin, D.G. Sarantites, L.G. Sobotka, P. Bhattacharyya, B.A. Brown, Nucl. Phys. A **682**, 22c (2001).